aerospace

MDPI

Article

Reverse Design of a Novel Coupling Strut for Vibration Attenuation in the Helicopter Cabin

Ming Ding, Jinhui Jiang *, Fang Zhang *, Xiao Liang and Nansun Shen

State Key Laboratory of Mechanics and Control of Mechanical Structures, Nanjing University of Aeronautics and Astronautics, Nanjing 210016, China

* Correspondence: jiangjinhui@nuaa.edu.cn (J.J.); zhangfangyy@163.com (F.Z.)

Abstract: Helicopter gearbox support strut is one of the main research objects in the field of vibration and noise control in helicopter cabins. Aiming to further widen the vibration attenuation range of traditional Bragg periodic struts, a novel type of Local resonance (LR)/Bragg coupling periodic strut with graded parameters as well as the reverse design method is proposed. Combined with the spectral element method (SEM) and the transfer matrix method (TMM), the analytical expression of the transform relationship of longitudinal vibrations through the coupling strut is yielded. The impacts of different parameters on the boundaries of bandgaps are explored according to the results of simulation analysis. On this basis, the gradient of parameters is determined, and then all unknown structural parameters can also be determined. Compared with the traditional Bragg periodic struts and the LR/Bragg coupling periodic strut with non-graded parameters, the presented strut has an obvious advantage of widening the low-frequency bandgaps below 500 Hz.

Keywords: LR/Bragg coupling strut; reverse design; helicopter cabin; spectral element method; transfer matrix method; vibration attenuation

check for updates

Citation: Ding, M.; Jiang, J.; Zhang, F.; Liang, X.; Shen, N. Reverse Design of a Novel Coupling Strut for Vibration Attenuation in the Helicopter Cabin. *Aerospace* **2022**, *9*, 843. https://doi.org/10.3390/aerospace9120843

Academic Editor: Rosario Pecora

Received: 2 November 2022
Accepted: 15 December 2022
Published: 18 December 2022

Publisher's Note: MDPI stays neutral with regard to jurisdictional claims in published maps and institutional affiliations.

Copyright: © 2022 by the authors. Licensee MDPI, Basel, Switzerland. This article is an open access article distributed under the terms and conditions of the Creative Commons Attribution (CC BY) license (https://creativecommons.org/licenses/by/4.0/).

1. Introduction

The noise level in the helicopter cabin is influenced by the rotor, tail rotor, engine, and transmission system. The complex composition of cabin noise leads to harsh riding condition, which seriously restricts the development and market expansion of helicopters [1,2]. After testing and analysis, the vibration transferring from the gearbox to the cabin is considered to be one of the main causes of high cabin noise level [3,4]. However, the attenuation of vibration by conventional support struts is negligible. The optimization and design of struts thus have been a popular area for researchers. In the past several decades, lots of efforts have been devoted to developing passive and active solutions to address this issue.

The core of the active solutions is the actuators controlled by active control algorithms. The current mainstream solution is to install actuators on the strut to provide external force to achieve vibration isolation [5–8]. In addition, the panel which is near to the mounting point of the strut is an optional location for actuator installation [9,10]. The active technology is usually effective in the simulation tests, but may not achieve the expected results in practical engineering applications due to various constraints, such as equipment failure, lack of power supply, and the instability of algorithms, etc. In addition, the active technique is more suitable for specific target frequencies or narrow-band vibration attenuation, and its application in wide-band vibration attenuation is not very satisfactory.

The main idea of the passive solutions is to install energy-consuming devices at appropriate locations in the main structure for energy conversion, thus reducing the vibration energy absorbed by the primary structure to achieve the purpose of vibration attenuation. Compared with active schemes, passive solutions are less costly and more effective in wide-band vibration attenuation. By far, the dynamic anti-resonance vibration isolation (DAVI) [11], consisting of elastic elements, damping elements, and inertial elements, is

one of the most popular passive solutions applied in engineering practices. The DAVI can counteract the excitation force by the elastic force generated by the elastic elements (e.g., springs) and the inertial force generated by the inertial elements (e.g., counterweight). Based on the DAVI systems above, the improved rotor isolation system (IRIS) [12], the SARIB [13] and the Liquid Inertia Vibration Eliminator (LIVE) [14] are all well-deployed in real helicopter engineering. For instance, the SARIB has also been successfully equipped in the NH-90 and Tiger helicopters. Recently, passive periodic struts are considered as the way to attenuate vibrations because of their wave filtering characteristic. The specific manifestation of this characteristic is that waves laid in some frequency ranges called stop bands cannot propagate along the periodic structures. Currently, there are two kinds of mechanisms for periodic structures to generate bandgaps, namely the Bragg scattering mechanism [15] and the local resonance (LR) mechanism [16]. Design and optimization of periodic Bragg strut applied in the gearbox systems of helicopters have been carried out in recent years. In order to attenuate the noise in helicopter cabin, Asiri, Baz and Pines [17–19] constructed a novel type of gearbox periodic struts which consists of five unit cells. An experiment was designed aiming to test vibration attenuation performance of the strut with a gearbox assembly, and the results showed that the strut performed well in broadband damping. Szefi, Smith and Lesieutre [20–24] tried to introduce embedded fluid elements to the layered isolator to enhance the performance of passive vibration isolation and succeed finally. Wang, Lu and Ma [25–28] combined two sets of Bragg struts in an ingenious way and yielded a novel type of composite strut. The strut performed well in vibration attenuation on the basis of satisfying the strength and stiffness constraints. However, current research are mainly based on the Bragg mechanism to design the struts, and there is almost no strut design using the LR mechanism. Meanwhile, the center frequency of the first Bragg stop band is inversely proportional to the length of cells of the periodic structures, namely, it is difficult for Bragg structures to meet the length requirements in the helicopter cabin while obtaining the low frequency stop band. This is why current studies on helicopter periodic struts have focused on reducing the mid- and high-frequency vibrations (500–2000 Hz). However, the vibrations below 500 Hz also have a great contribution to the noise environment in the cabin and should not be ignored.

The LR mechanism first proposed by Liu et al. [29] paved a new way towards this problem. They developed 3D phononic crystals consisting of a cubic array of coated spheres dipped in an epoxy matrix. The frequency range of the LR stopband is lower than the Bragg stopband, while they have the same characteristic size. This pioneering work provides a new research direction in the field of periodic structures and phononic crystals, and many scholars have made a lot of achievements in this direction [30–37]. The LR structures are always constructed with the intention of introducing locally resonant substructures into matrix materials, and they can be implemented in the context of vibration control engineering. Low-frequency resonance gaps can be achieved in structural elastic waveguides such as rods, beams, plates, shells, etc. by installing local resonators periodically. In traditional vibration control engineering, the idea of multi-frequency resonance has been widely used in the design of broadband vibration absorbers [38–42]. For example, when designing a vibration attenuation scheme for suppressing the vibration response of a lumped parameter system, a set of single-degree-of-freedom (SDOF) vibration absorbers with slightly staggered resonant frequencies can be considered. The great acting force is generated by these vibration absorbers in the vicinity of multiple resonant frequencies, so as to achieve the purpose of broadening the vibration reduction frequency band [39,41]. Similarly, a group of SDOF vibration absorbers with slightly staggered resonant frequencies are distributed on a continuous structure, which can realize broadband vibration reduction of continuous structures [38,40]. It can be considered that the graded design based on the reasonable selection of parameter is an effective way to achieve broadband vibration attenuation. Introducing vibration absorbers with multi-frequency resonance into the design of the coupling strut is expected to further widen the stop bands.

In this paper, we construct a novel type of LR/Bragg coupling periodic strut by adding local resonators to the periodic arranged strut, aiming to further widen the bandgap from the combination of the LR mechanism and the Bragg mechanism. In Section 2, the formulas for calculating the propagation constant of the infinite strut and displacement/force transmissibility through finite struts are derived. Section 3 is devoted to investigating the variation law of the bandgap boundaries with parameters of resonators, which provides theoretical guidance for the subsequent work. The graded design formed by the combination of different unit cells is introduced to widen the existing bandgap. We finish with some concluding remarks in Section 4.

2. Dynamic Model and Analysis Method

For facilitating analysis without losing generality, our study starts with the periodic struts with two resonators in each unit cell. Two strut configurations are considered, that is, the periodic arranged strut with series resonators and parallel resonators. The infinite discrete models of two configurations are shown in Figure 1. Considering the space and weight limitations in the helicopter cabin, we decided to take the strut with parallel resonators as the research objective. Each unit cell of the strut is composed of a metal layer (denoted by the symbol A) and a rubber layer (denoted by the symbol B), and two parallel resonators are attached to the metal layer also. One of the resonators is connected to the top side of layer A by default, and the rest of the resonators can be attached to any location on layer A except the top side. The choice of the location of the second resonator will be discussed in detail in Section 3.1. For the strut studied in this paper, it is assumed that all interfaces between the connected layers is ideal.

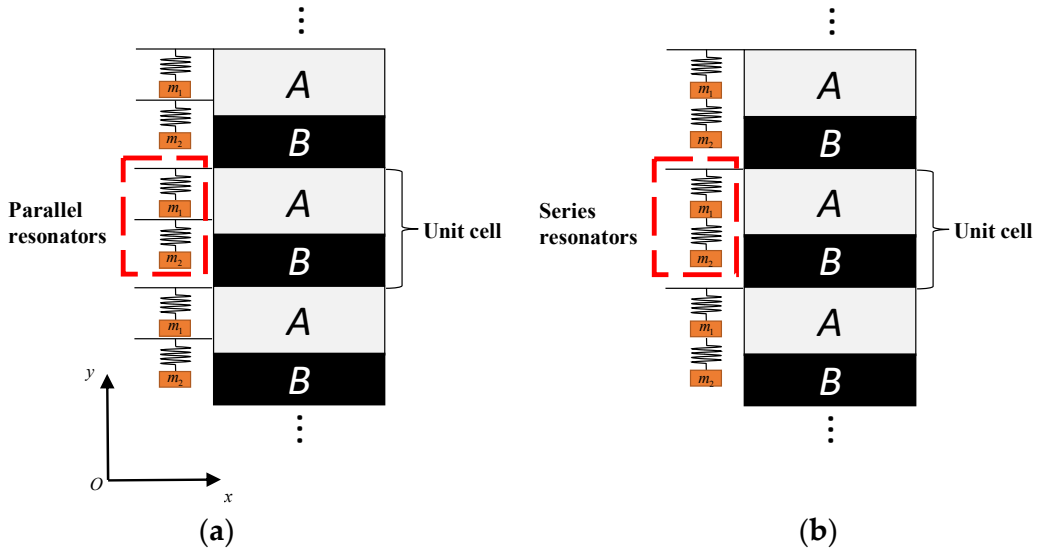


Figure 1. Configuration diagrams of the infinite struts with local resonators: (**a**) parallel resonators (**b**) series resonators.

2.1. Governing Equation for Longitudinal Wave Propagation

Consider an LR unit cell consisting of a uniform rod unit and a resonator, as sketched in Figure 2. k and m represent the stiffness and mass of the resonator, and L is the length of the rod.

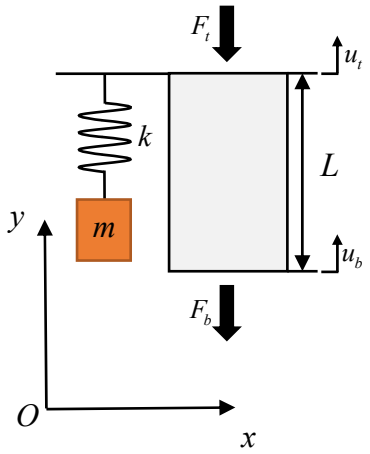


Figure 2. Configuration diagram of the rod unit attached with a resonator.

2.1.1. Rod without Resonators

For the rod unit without resonators, the equation of motion can be expressed in the following form:

$$\rho S\frac{\partial^2 u(y,t)}{\partial t^2} - ES\frac{\partial^2 u(y,t)}{\partial y^2} = 0 \tag{1}$$

where ρ and S denote the density and cross-sectional area of the rod unit, respectively. E is the Young's modulus, and $u(y,t)$ is the displacement along the x-direction. The solution of Equation (1) can be expressed as

$$u(y,t) = U(y)e^{-i\omega t} \tag{2}$$

where ω is the circular frequency of harmonic motion. Substituting Equation (2) into Equation (1), we get

$$E\frac{\partial^2 U(y)}{\partial y^2} + \omega^2\rho U = 0 \tag{3}$$

The solution of Equation (3) is

$$U(y) = A_1e^{-i\beta(L-y)} + A_2e^{-i\beta y} \tag{4}$$

where $\beta = \omega\sqrt{\rho/E}$ is the number of longitudinal waves, and L represents the length of the rod unit. Substituting the boundary conditions into Equation (4), the coefficients A_1 and A_2 can be calculated. Defining the nodal displacements at the top and bottom sides of the rod unit as U_t and U_b, namely

$$U_b = U|_{(y=0)}, U_t = U|_{(y=L)} \tag{5}$$

The coefficients A_1 and A_2 can be expressed as

$$\begin{bmatrix} A_1 \\ A_2 \end{bmatrix} = \frac{1}{1-e^{-i2\beta L}}\begin{bmatrix} 1 & -e^{-i\beta L} \\ -e^{-i\beta L} & 1 \end{bmatrix}\begin{bmatrix} U_t \\ U_b \end{bmatrix} \tag{6}$$

According to Equations (3) and (6), the spectral displacement $U(y)$ can be rewritten as

$$U(y) = N_t(y)\overline{U}_t + N_b(y)\overline{U}_b \tag{7}$$

where $N_t(y) = \frac{1}{1-e^{-i2\beta L}}e^{-i\beta(L-y)} + \frac{-e^{-i\beta L}}{1-e^{-i2\beta L}}e^{-i\beta y}$ and $N_b(y) = \frac{-e^{-i\beta L}}{1-e^{-i2\beta L}}e^{-i\beta(L-y)} + \frac{1}{1-e^{-i2\beta L}}e^{-i\beta y}$ are shape functions.

Similarly, the internal force $f(y,t)$ also can be expressed as

$$f(y,t) = F(y)e^{-i\omega t} \tag{8}$$

In the frequency domain, the internal force and the displacement have the following relationship:

$$F(y) = ES\frac{\partial U(y)}{\partial y} \tag{9}$$

Defining the nodal forces at the top and bottom sides of the rod unit as F_t and F_b, namely

$$F_b = F|_{(y=0)}, F_t = F|_{(y=L)} \tag{10}$$

Substituting Equation (7) and Equation (9) into Equation (10), we obtain

$$\begin{bmatrix} F_t \\ F_b \end{bmatrix} = \mathbf{D}\begin{bmatrix} U_t \\ U_b \end{bmatrix} = \frac{ES i\beta}{(1-e^{-i2kl})}\begin{bmatrix} 1+e^{-i2kl} & -2e^{-ikl} \\ -2e^{-ikl} & 1+e^{-i2kl} \end{bmatrix}\begin{bmatrix} U_t \\ U_b \end{bmatrix} \tag{11}$$

where **D** is the dynamic stiffness matrix of the rod unit, and it can be rewritten as Equation (12) according to Euler's formula [43,44].

$$\mathbf{D} = \begin{bmatrix} D_{11} & D_{12} \\ D_{21} & D_{22} \end{bmatrix} = \frac{ES\beta}{\sin(\beta L)}\begin{bmatrix} \cos(\beta L) & -1 \\ -1 & \cos(\beta L) \end{bmatrix} \tag{12}$$

2.1.2. Rod with Resonators

When a resonator is attached to the rod unit, the effect of the resonator on the rod can be equivalent to the external force acting on the connection boundary, and then the equivalent transfer matrix (TM) relationship of the cell can be deduced. The inertial force generated by longitudinal vibration of the resonator will be transmitted to the rod, and the reaction force can be expressed as

$$F_r = D_r U_t \tag{13}$$

where $D_r = \frac{-m\omega^2 k}{k-m\omega^2} - m_0\omega^2$ is the dynamic stiffness of the resonator, and m_0 is the additional mass of the spring in practical engineering applications [45]. We can get the relation between the force responses and displacements at two ends of the cell:

$$\begin{bmatrix} F_t \\ F_b \end{bmatrix} = \mathbf{D}\begin{bmatrix} U_t \\ U_b \end{bmatrix} = \begin{bmatrix} D_{tt} & D_{tb} \\ D_{bt} & D_{bb} \end{bmatrix}\begin{Bmatrix} U_t \\ U_b \end{Bmatrix} = \begin{bmatrix} D_{11}+D_r & D_{12} \\ D_{21} & D_{22} \end{bmatrix}\begin{bmatrix} U_t \\ U_b \end{bmatrix} \tag{14}$$

where **D** is the dynamic stiffness matrix of the LR unit by combining the dynamic stiffnesses of the rod unit and the resonator, F_t, F_b and U_t, U_b respectively define the force and displacements, in where the subscripts t and b represent the top and bottom sides of the unit. Equation (14) can be rearranged as

$$\begin{bmatrix} U_b \\ F_b \end{bmatrix} = \begin{bmatrix} -D_{tb}^{-1}D_{tt} & D_{tb}^{-1} \\ D_{bt} - D_{bb}D_{tb}^{-1}D_{tt} & D_{bb}D_{tb}^{-1} \end{bmatrix}\begin{bmatrix} U_t \\ F_t \end{bmatrix} \tag{15}$$

Imposing continuity and compatibility of contact interfaces between adjacent layers, we get:

$$\begin{bmatrix} U_t' \\ F_t' \end{bmatrix} = \begin{bmatrix} U_b \\ -F_b \end{bmatrix} = \begin{bmatrix} -D_{tb}^{-1}D_{tt} & D_{tb}^{-1} \\ -D_{bt} + D_{bb}D_{tb}^{-1}D_{tt} & -D_{bb}D_{tb}^{-1} \end{bmatrix}\begin{bmatrix} U_t \\ F_t \end{bmatrix} = \mathbf{T}\begin{bmatrix} U_t \\ F_t \end{bmatrix} \tag{16}$$

where **T** is the TM of the cell, and U_t' and F_t' define the force and deflections states of the top side of the next cell. The explicit expression for the **T** is given by

$$\mathbf{T} = \begin{bmatrix} \cos(\beta L) + (D_r/ES\beta)\sin(\beta L) & -(ES\beta)^{-1}\sin(\beta L) \\ ES\beta\sin(\beta L) - D_r\cos(\beta L) & \cos(\beta L) \end{bmatrix} \tag{17}$$

Consider the LR rod unit cell containing two parallel resonators, as shown in Figure 3, the original cell can be separated into corresponding sub cells with single-resonator separately. Thus, the TM of the entire unit can be obtained by the continuous condition of the contact interface:

$$\mathbf{T}_{cell} = T_{II} \times T_I \tag{18}$$

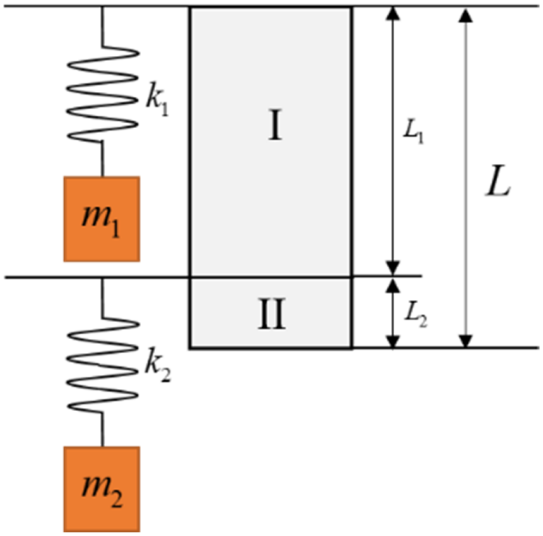


Figure 3. Configuration diagram of the rod unit attached with two resonators.

The transfer matrices of layer A and layer B are shown in Figure 1 can be obtained easily by Equations (17) and (18). According to the principle of superposition, the TM of the entire cell consisting of layer A and layer B can be expressed as

$$\mathbf{T}_{cell} = T_B \times T_A \tag{19}$$

2.2. Propagation Constant of the Infinite Periodic Strut

For an infinite periodic strut, the relationship of state vectors of adjacent cells can be obtained by Bloch theorem [46] and Equation (16):

$$\begin{bmatrix} U_b \\ F_b \end{bmatrix}_b = \mathbf{T}_{cell} \begin{bmatrix} U_t \\ F_t \end{bmatrix}_a = \lambda \begin{bmatrix} U_t \\ F_t \end{bmatrix}_a \tag{20}$$

Here, $\lambda = e^{\mu}$ or $\lambda = e^{-\mu}$, which represents a pair of positive-going or negative-going characteristic waves. μ is called the propagation constant. The real part of μ is defined as the attenuation coefficient, and it represents the attenuation degree of the amplitude of the wave. The imaginary part of μ is defined as the phase coefficient, and it represents the phase difference of the wave motion in adjacent periodic units. Equation (20) can be rewritten as

$$\left(\mathbf{T}_{cell} - e^{\pm\mu} \cdot \mathbf{I}\right) \begin{bmatrix} U_t \\ F_t \end{bmatrix}_a = \begin{bmatrix} T_{c11} - e^{\pm\mu} & T_{c12} \\ T_{c21} & T_{c22} - e^{\pm\mu} \end{bmatrix} \begin{bmatrix} U_t \\ F_t \end{bmatrix}_a = 0 \tag{21}$$

where T_{c11}, T_{c12}, T_{c21} and T_{c22} are the elements of matrix $\mathbf{T}_{cell}$. Thus, $e^{\pm\mu}$ are the eigenvalues of matrix $\mathbf{T}_{cell}$. As $e^{-\mu} + e^{\mu} = 2\cosh(\mu)$, we have

$$\cosh(\mu) = \frac{e^{-\mu} + e^{\mu}}{2} = \frac{T_{c11} + T_{c22}}{2} \tag{22}$$

2.3. Vibration Transmission of the Finite Strut

For a finite periodic coupling strut, the overall TM of the strut $\mathbf{T}_{strut}$ can be obtained by multiplying the transfer matrices of the individual cells:

$$\mathbf{T}_{strut} = \prod_{i=1}^{n} \mathbf{T}_{cell_i} \tag{23}$$

in which n is the number of cells. It is worth mentioning that Equation (23) is also applicable to calculate the transmission of a disordered or near-periodic strut, whose cells have distinct transfer matrixes.

Imposing continuity and compatibility at the bottom side of the unit cell yields

$$\begin{bmatrix} U_t \\ F_t \end{bmatrix}^{n+1} = \begin{bmatrix} U_b \\ -F_b \end{bmatrix}^{n} = \mathbf{T}_{strut} \begin{bmatrix} U_t \\ F_t \end{bmatrix}^{1} = \begin{bmatrix} T_{s11} & T_{s12} \\ T_{s21} & T_{s22} \end{bmatrix} \begin{bmatrix} U_t \\ F_t \end{bmatrix}^{1} \tag{24}$$

Where T_{s11}, T_{s12}, T_{s21} and T_{s22} are the elements of matrix $\mathbf{T}_{strut}$, and the superscripts of vectors denote the serial number of the cell. The displacement and force transmissibility of the finite strut can be obtained with two different boundary conditions.

(1) Free-Free Condition

When both ends of the strut are in free condition, the force and displacements of the two ends can be expressed as

$$\begin{cases} U_t \neq 0, & F_t = f_0 \\ U_b \neq 0, & F_b = 0 \end{cases} \tag{25}$$

where f_0 is the external excitation acting on the top of the strut. Combining Equations (23) and (24), we can get the displacement transmissibility of the finite periodic structure:

$$T(f) = |U_b/U_t| = \left| T_{s11} - T_{s12} T_{s22}^{-1} T_{s21} \right| \tag{26}$$

(2) Fix-Fix Condition

When both ends of the strut are in fix condition, the force and displacements of the two ends can be expressed as

$$\begin{cases} U_t \neq 0, & F_t = f_0 \\ U_b = 0, & F_b \neq 0 \end{cases} \tag{27}$$

where f_0 is the external excitation acting on the top of the strut. Combining Equations (23) and (26), we can get the force transmissibility of the finite periodic structure:

$$T(f) = |f_b/f_t| = \left| T_{s22} - T_{s21} T_{s11}^{-1} T_{s12} \right| \tag{28}$$

Considering that the periodicity of the strut will be broken since the subsequent graded design, in order to directly compare the wave attenuation capability of the finite disordered strut with that of the infinite disordered strut, we adopt the supercell method which has been widely used in the study of defect states in phononic crystals [47], to characterize the bandgap characteristics of the finite strut. The so-called supercell method is to regard the whole disordered structure with finite periods as a supercell and introduce periodic boundary conditions at both ends of the supercell to calculate its band gap characteristics. From this point of view, the matrix $\mathbf{T}_{strut}$ of the whole disordered structure can be obtained by Equation (23), and the propagation constant μ can be calculated based on Equations (21) and (22). The transmission characteristics reflected by μ are expected to be mostly matched with that of the finite disordered strut.

3. Simulation Analysis and Results Discussion

3.1. Illustrative Example

In this subsection, a finite coupling periodic strut is designed to verify the theoretical calculation results of the method presented in this paper. The results obtained by the present method are compared with those obtained by the finite element software. The typical Bragg strut studied in [17,26] is taken as the prototype model, and five groups of parallel resonators are added to the strut. The simplified diagram of the finite coupling strut is given in Figure 4. The proposed coupling strut is composed of five identical unit cells, and every cell is made up of an aluminum layer carrying two parallel resonators and a rubber layer. An aluminum layer is added to the bottom of the strut for ease of installation. A ring-shaped rubber layer and a ring-shaped lead block comprise the resonator. In the simulation analysis, the input excitation is applied at the center point of the top aluminum layer, and the output signal is measured at the center point of the bottom aluminum layer. The boundary conditions at both ends of the strut are free, and the transmissibility is defined as

$$T = 20 \log \left| \frac{U_b}{U_t} \right| \tag{29}$$

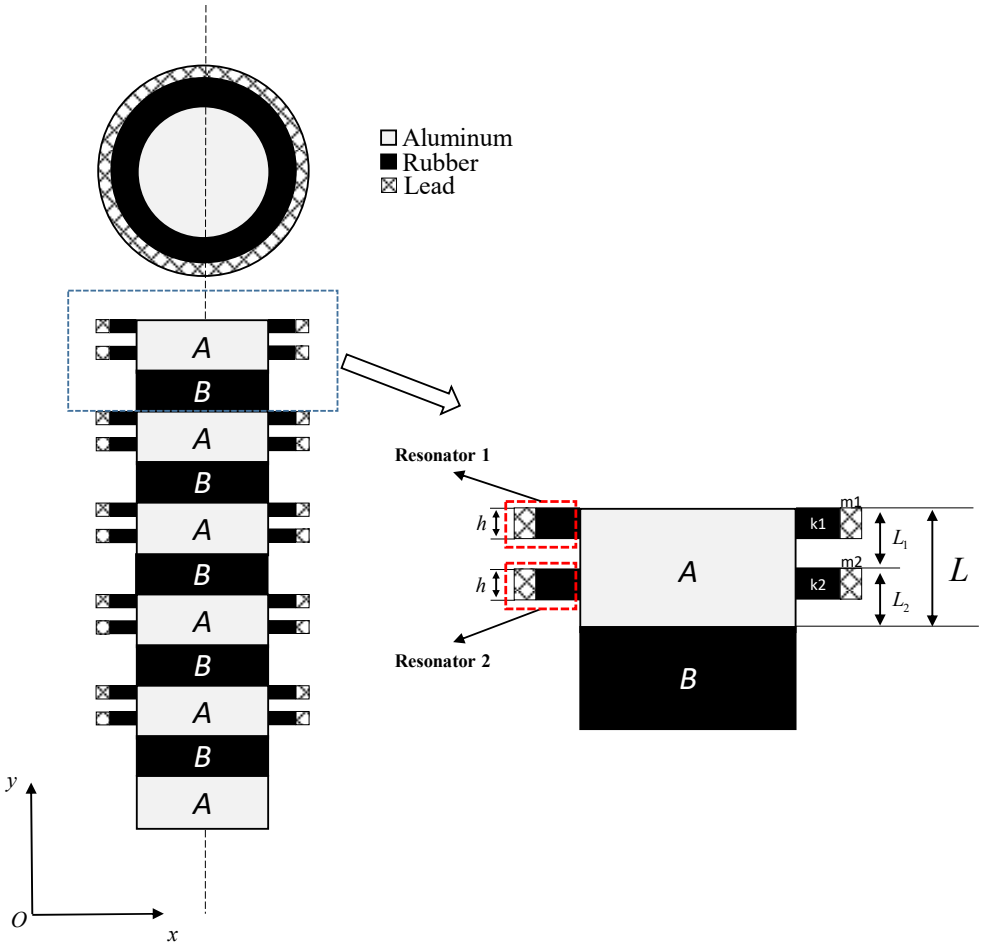


Figure 4. Schematic representation of a finite coupling periodic strut.

When the longitudinal wave propagates in the strut, the lead block will vibrate in the longitudinal direction, and the cylindrical rubber layer will undergo shear deformation. The resonator can be simplified as a mass–spring system, and the longitudinal stiffness of the rubber layer can be approximately expressed as [48]

$$k = 2\pi Gh/(\ln R_{out} - \ln R_{in}) \tag{30}$$

where G is shear modulus of the rubber, and h denotes the longitudinal thickness of rubber layer. R_{out} and R_{in} are the outer radius and inner radius of the rubber layer, respectively. The parameters of prototype strut used in the simulation are the same as the ones given in [26]. Considering the weight constraints in the practical design, it is assumed that the ratio of the mass of the resonators to that of the prototype strut has a constrained maximum value. Therefore, the mass ratio is set to be 0.8 in the subsequent numerical samples. The material properties and sizes of the components of the coupling strut are listed in Tables 1 and 2. The mass and equivalent stiffness of the two resonators can be calculated according to known parameters, i.e., m_1 = 0.0273 kg, m_2 = 0.0410 kg, k_1 = 93,368.56 N/m and k_2 = 93,368.56 N/m. The resonance frequencies of the two resonators are calculated to be 294.16 Hz and 240.18 Hz by Equation (31), respectively.

$$f_i = (1/2\pi) \times (k_i/m_i)^{1/2} (i = 1, 2) \tag{31}$$

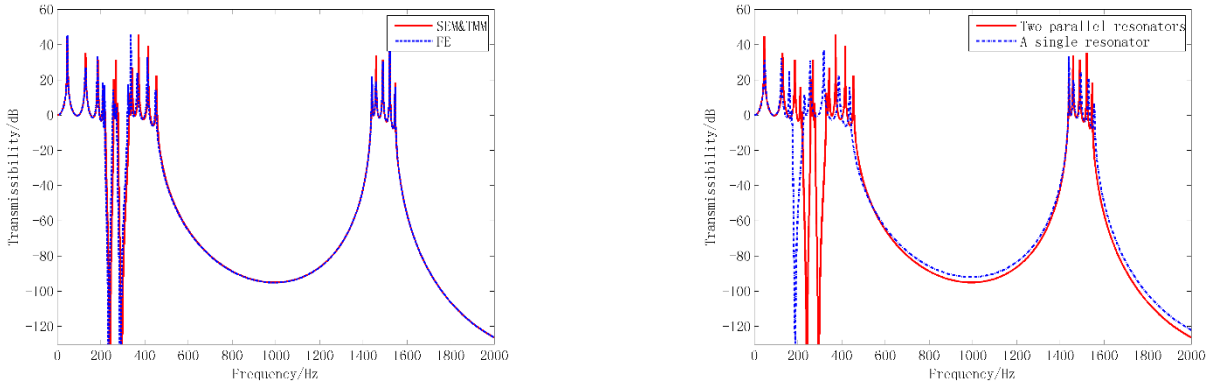
Table 1. Properties of materials.

	Materials	**Density /kg·m^{-3}**	**Elastic Modulus /GPa**	**Shear Modulus /Gpa**
Parameters of the rod	Aluminum	2700	73	28.7
	Rubber	1291	0.0024	0.001
Parameters of the resonators	Rubber	1291	0.0024	0.001
	Lead	11,600	40.8	14.9

Table 2. Sizes of the components of the coupling strut.

Part	**Material**	**Inner Radius /m**	**Outer Radius /m**	**Length/m**
Rod	Aluminum	\	0.025	0.02
	Rubber	\	0.0215	0.015
Resonator 1	Rubber	0.0250	0.0350	0.005
	Lead	0.0350	0.0371	0.005
Resonator 2	Rubber	0.0250	0.0350	0.005
	Lead	0.0350	0.0381	0.005

The results given in Figure 5 show that the transmissibility of the strut achieved by the presented algorithm (red line) agrees well with that obtained by the finite element software (blue dotted line). Thus, the accuracy of the proposed algorithm and the simplified model of the resonator is validated. Two typical asymmetric LR gaps can be observed below 500 Hz with sharp attenuation at the resonance frequencies of the two resonators, and two typical symmetrical and smoothly falling Bragg gaps lie in the range of 500–2000 Hz. Although the LR mechanism has more advantages in low-frequency vibration control obviously, it has the problem of narrow bandgap. In addition, the transmission characteristics of the strut with single resonator and that with two resonators are also compared in Figure 5b. The parameters are the same as in the preceding example, with the only difference that the two parallel resonators have been replaced by a single resonator with the same total mass of lead. The resonance frequency is tuned to 186.04 Hz, and correspondingly, the LR stop gaps also degenerate into one. The calculated mass and equivalent stiffness of the resonators are summarized in Table 3. It can be seen from Figure 5b that the parallel resonators have an advantage over the single resonator in multi-frequency vibration attenuation.



(**a**) (**b**)

Figure 5. Transmission capability of struts: (**a**) obtained by proposed method and finite element software (**b**) with two parallel resonators and a single resonator.

Table 3. Calculated parameters of the resonators.

		Mass /kg	Equivalent Stiffness /N·m^{-1}	Resonance Frequency /Hz
Parallel resonators	Resonators 1	0.0273	93,368.56	294.16
	Resonators 2	0.0410	93,368.56	240.18
Single resonator		0.0683	93,368.56	186.04

3.2. Parametric Influence Study

We only take into account several particular struts with carefully selected system parameters in the previous subsection. The impacts of designing parameters of the resonators on the bandgap behavior, including the location, width, and attenuation capabilities of all the bandgaps, will be of great relevance in the practical design, nevertheless. It is obvious that the mass, stiffness and spacing of resonators dominate the variation of wave propagation while the parameters of the rod are constant. In order to acquire a more thorough understanding of how bandgap boundaries vary with the configuration of resonators, the ratio parameters are determined by $\theta = m_2/m_r$, $\eta = k_2/k_1$ and $\varsigma = L_2/L_A$, respectively, and the range of the parameters can be obtained as $\theta \in [0,1]$, $\eta \in [0,+\infty)$ and $\varsigma \in [0,1]$. m_r represents the total mass of lead of two resonators. All simulation analysis in this section is carried out with the assumption of infinite periodicity, and the analyzed frequency range in all examples is set to 0–2000 Hz.

The effect of the spacing ratio on the variation of the bandgap boundaries is considered first. Several band diagrams are displayed in Figure 6, and the boundaries of the first to fourth stopbands are signed by red, blue, green and black symbols, respectively. The detailed parameters are stated in the caption. Figure 6 shows that the bandgap boundaries remain unchanged due to the variation of ς, therefore the variation of ς will not be considered hereafter and it will be set to be 0.5 in the following examples.

Next, the band diagrams are displayed in Figures 7 and 8, where the variation of bandgap boundaries taking θ and η as the independent variable, respectively. The boundaries of the first to fourth stopbands are also signed by red, blue, green and black symbols, respectively.

There are several special situations in Figures 7 and 8 which need to be discussed separately. When θ or η takes the value of 0 or 1, namely the amount of the resonators in every cell is reduced to one, leading the degeneration of the number of LR bandgaps to one. Meanwhile, it should not be ignored that when the resonance frequencies of the two resonators are the same, e.g., $\theta = 0.5$ in Figure 7b and $\eta = 1$ in Figure 8b, the upper border of the first bandgap reaches the lower border of the second bandgap at the point. It can be easily found that the top boundary of the second bandgap rises much faster than that of the lower border when away from the point, namely the width of the second band

gap tends to increase fast. The boundaries of the third bandgap change in the opposite way. It is also evident that the passband between the third bandgap and the fourth bandgap hardly changes with the variation of the variables in most cases.

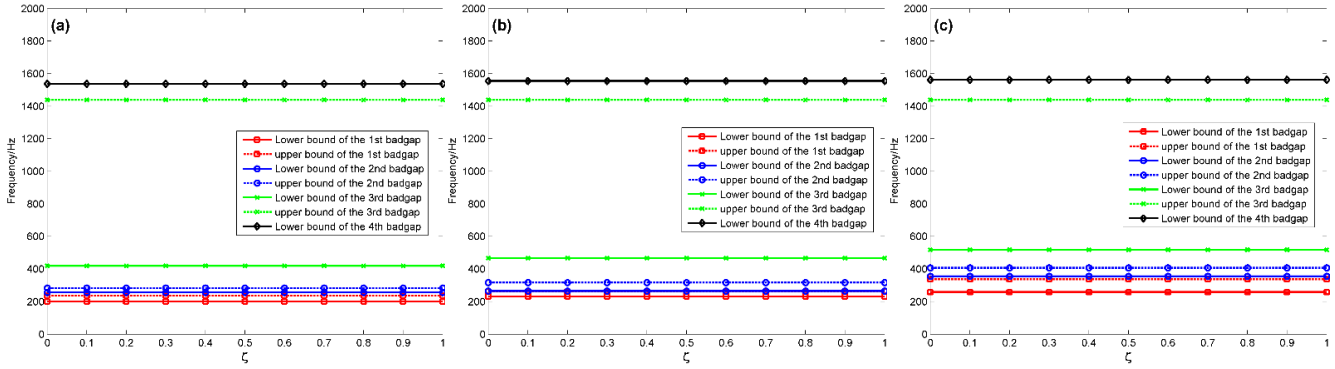


Figure 6. Lower and upper borders of the bandgaps for the infinite coupling strut: (**a**) as a function of ς when $\theta = 0.25$ and $\eta = 0.5$; (**b**) as a function of ς when $\theta = 0.5$ and $\eta = 1$; (**c**) as a function of ς when $\theta = 0.75$ and $\eta = 2$.

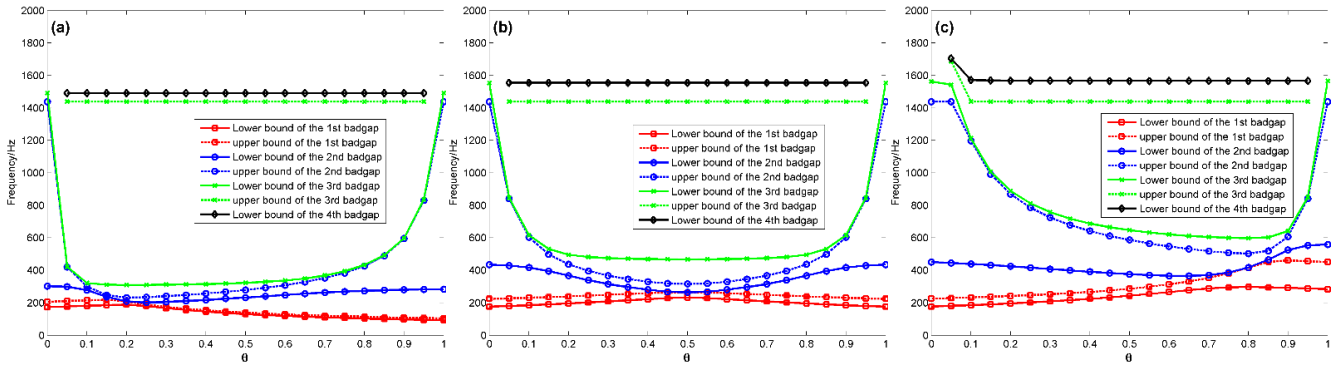


Figure 7. Lower and upper borders of the bandgaps for the infinite coupling strut: (**a**–**c**) as a function of θ when $\eta = 0.25$, $\eta = 1$ and $\eta = 4$, respectively.

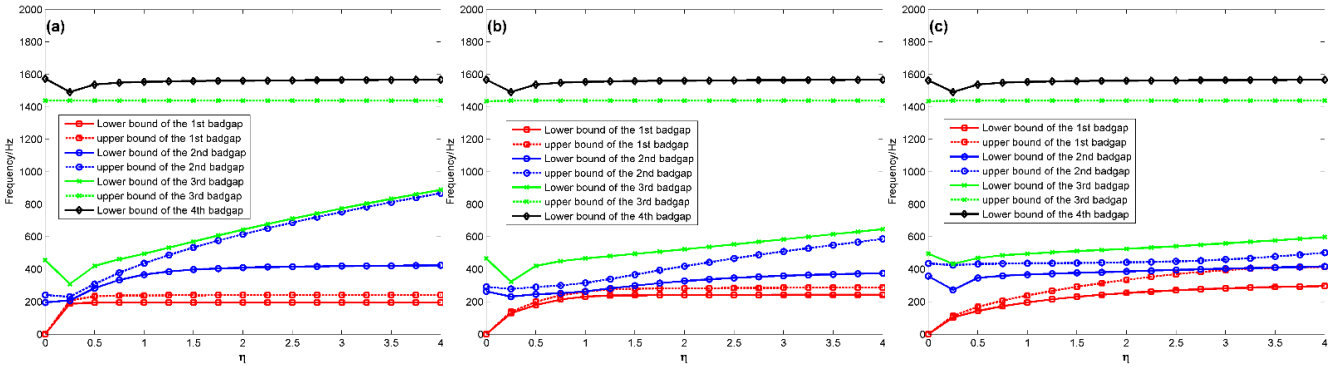


Figure 8. Lower and upper borders of the bandgaps for the infinite coupling strut: (**a**–**c**) as a function of η when $\theta = 0.2$, $\theta = 0.5$ and $\theta = 0.8$, respectively.

In conclusion, the overlap of bandgaps of the infinite strut may happen when parameters of resonator change. In the condition of efficiently leveraging the overlap of bandgap boundaries, a graded designed coupling strut has the potential to further broaden the bandwidth. This finding motivates us to further attempt to combine units whose parameters are distributed in gradients to increase the bandwidth.

3.3. Reverse Design

The work of several researchers [25,49–51] affirm that the vibration-attenuation frequency ranges on the vibration transmission curve of finite structure correspond to those of the infinite periodic structure, even if the finite structure composed of only a few cells. Hence, the process of unit cell of infinite structures design is sufficient for the design of finite periodic structures. In this subsection, the continuous model in Section 3.1 is taken as the prototype model, and the analysis results in Section 3.2 is taken as a guide. With the goal of widening the band gap as much as possible below 500 Hz, the parameters of the resonators can be reversely determined.

It can be clearly observed that the band structure of the infinite periodic strut exhibits different sensitivities to mass ratio θ and stiffness ratio η. Thus, two graded approaches corresponding to these two parameters should be considered. For the two types of graded structures, the total bandgap after overlapping combination is the key point in the design and the main indicator of evaluation.

Under the same theoretical model and parameter environment as Figure 7b, the overlapping and broadening of band gaps after using graded mass ratio is studied. The total bandgap of a graded designed structure is actually the union of the upper and lower bandgaps of each graded unit. In order to more intuitively judge whether the band gaps generated by graded θ overlap with another, the distributions of the first to fourth band gaps are represented by red, blue, green and black bars in Figure 9a. As depicted in Figure 9a, the mass ratio θ lying in the intervals of $[0.1, 0.9]$ would create a broad overall bandwidth, whose range is 176–1439 Hz. Similarly, following the theoretical model in Figure 8b, it is evident from Figure 9b that a broad overall bandwidth within the range of 130–1439 Hz would be generated when η lying in the intervals of $[0.25, 2]$. In addition, the passband between the third bandgap and the fourth bandgap always exists and is hardly affected by the resonator parameters.

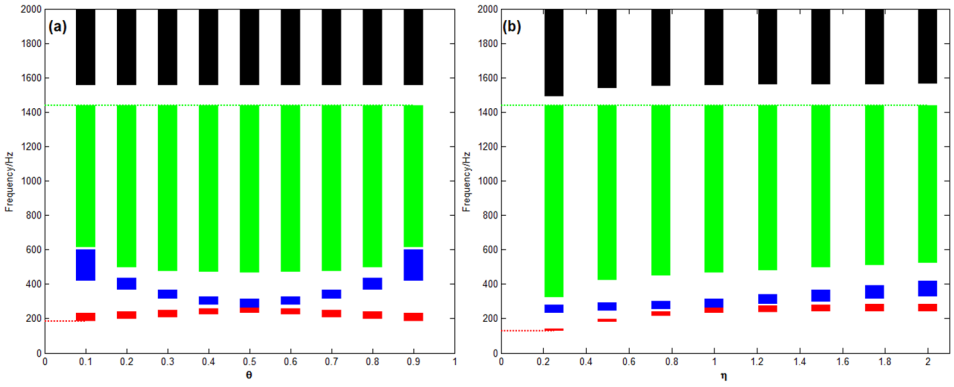


Figure 9. The bandgaps generated by the union of graded units, with the graded ranges of (**a**) $\theta \in [0.1, 0.9]$ when $\eta = 1$ and (**b**) $\eta \in [0.25, 2]$ when $\theta = 0.5$.

What should be emphasized is that the broad overall bandwidth obtained in the earlier part of this subsection are ideal results guaranteed by the premise of infinite periodicity. However, the actual structures with graded design constraints on the number of unit cells due to the space or weight requirement. The infinite strut studied in this paper has only 5 unit cells, what means that we can only select up to five different graded parameters for graded design. When the value of η is fixed to 1, the bandgap structure exhibits symmetry with respect to $\theta = 0.5$ in Figure 9a, thus reasonable parameters selected within the intervals of [0.1–0.5] can produce the broad overall bandwidth. Meanwhile, it is not hard to find in Figure 9b that the range of the bandgaps is not continuous enough to produce an overall broad bandgap by five graded parameters of η. Thus, we finally decide to use θ as the independent variable to construct the strut. The gradient of θ is finally set to {0.1, 0.2, 0.3, 0.4, 0.5} and $\eta = 1$. The finite continuous model constructed in Section 3.1 is selected as the

prototype model to be designed. The mass distribution of the resonators in the five unit cells is modified according to the decided gradient of θ, and the outer radii of lead calculated by θ and other known parameters are shown in Table 4. All the other parameters are the same as those in Tables 1 and 2. In order to show the graded design strut more intuitively, the rainbow segmentation schematic of the corresponding models and schematic diagram of unit cell are shown in Figures 10b and 10a, respectively. The aluminum layer added to the bottom of the strut is for ease of installation.

Table 4. Calculated parameters of the resonators in each cell.

	Cell 1	Cell 2	Cell 3	Cell 4	Cell 5
Outer radius of lead of resonator1/m	0.0395	0.0391	0.0386	0.0381	0.0376
Outer radius of lead of resonator 2/m	0.0355	0.0361	0.0366	0.0371	0.0376

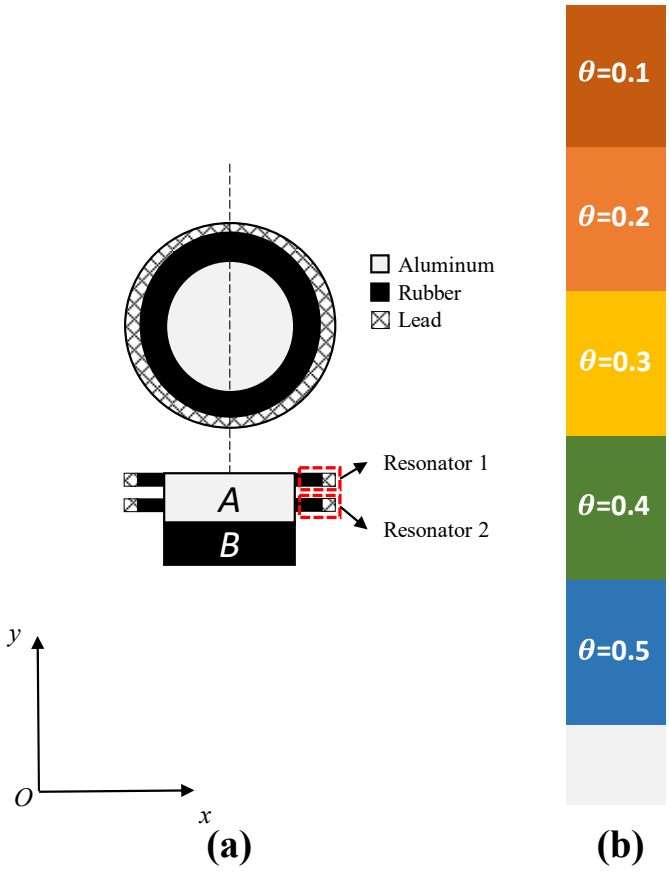


Figure 10. Diagrammatic sketches of the continuum strut by reverse design: (**a**) General schematic diagram of unit cells. (**b**) Rainbow segmentation schematic of the strut with graded parameter θ.

The vibration transmittance of the reverse designed strut and the corresponding attenuation constant curve are depicted in Figure 11a,b. The transmissibility of the designed strut shows the same trend of change as the attenuation constant of the corresponding supercell. It can be known from Figure 11 that the starting frequency of the vibration attenuation for the reverse designed strut is reduced to 187 Hz, which is very close to the 176 Hz predicted by the infinite strut. However, the broad coupling bandgap is not generated because the finite strut fails to satisfy the ideal periodic conditions, resulting that several resonance peaks still exist in the range of 200–500 Hz. It is worth mentioning that the results above are obtained in the absence of any damping of the structure and resonators. In vibration and noise control engineering, damping is often used to suppress

the peaks of the vibration response. Thus, the damping of structure and resonators is introduced to further improve the vibration attenuation performance of the strut.

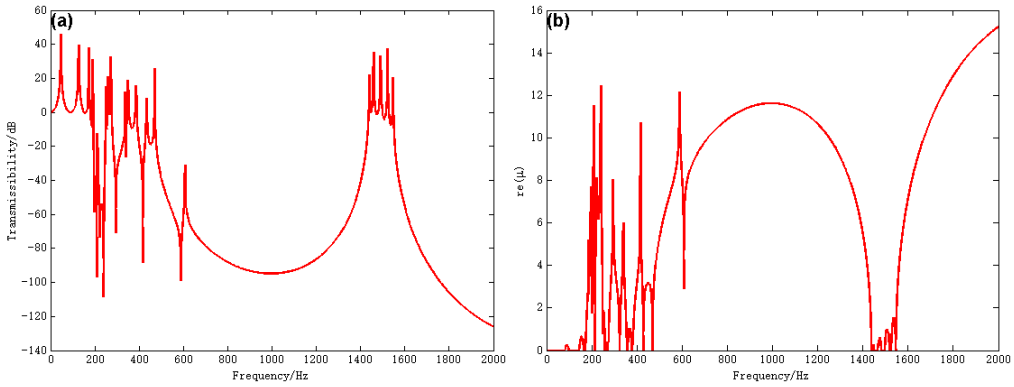


Figure 11. Band gap behavior of the reverse designed strut. (**a**) Transmission capability of the finite strut. (**b**) Attenuation constant of corresponding supercell.

Since the damping of metal is very small, only the damping of the rubber in the matrix strut and the resonators is considered. The material damping of rubber in the matrix strut and the resonators is, respectively, introduced by taking the form of complex Young's modulus $E(1 + i\delta)$ and complex stiffness $k(1 + i\delta)$, and δ represents the loss factor. The band gap behavior of the reverse designed strut with different damping is shown in Figure 12. It can be seen that after the introduction of damping, the resonance peaks in the entire frequency range (including the passband) are suppressed, and as the frequency increases, the peak suppression becomes more obvious.

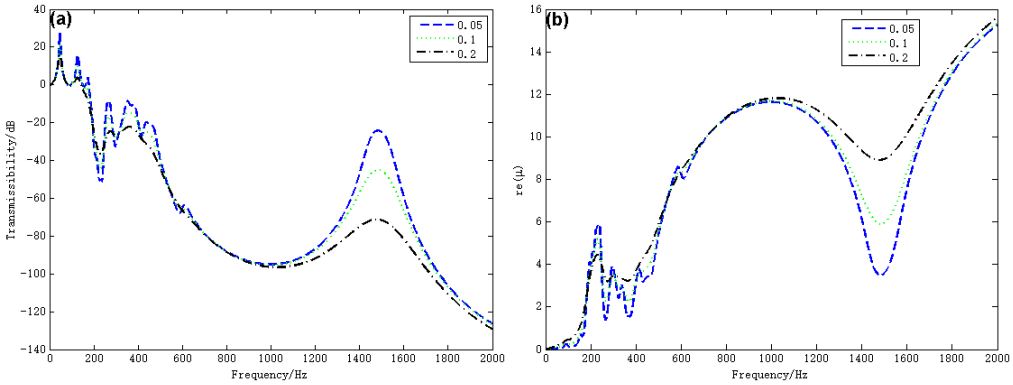


Figure 12. Band gap behavior of the reverse designed struts with different damping. (**a**) Transmission capability of the finite strut. (**b**) Attenuation constant of corresponding supercell.

Figure 13 shows the vibration transfer characteristics of the three types of struts when the loss factor is 0.1. The properties of materials and sizes of struts are the same as those illustrated in Tables 1–4. The coupling strut without graded design has a significant attenuation of vibration from 174 Hz to 268 Hz, and the attenuation reaches a maximum value of 63.21 dB at 210 Hz, which nears the resonance frequency (209.40 Hz) of the resonator. However, the attenuation effect of the strut for vibration in the range of 268 Hz to 500 Hz is not satisfactory. The transmissibility curve of the coupling strut without graded design shows that although the periodic attachment of the absorbers with the same resonant frequency improves the performance of vibration attenuation near the resonant frequency, it is hard for the strut to achieve broadband vibration attenuation.

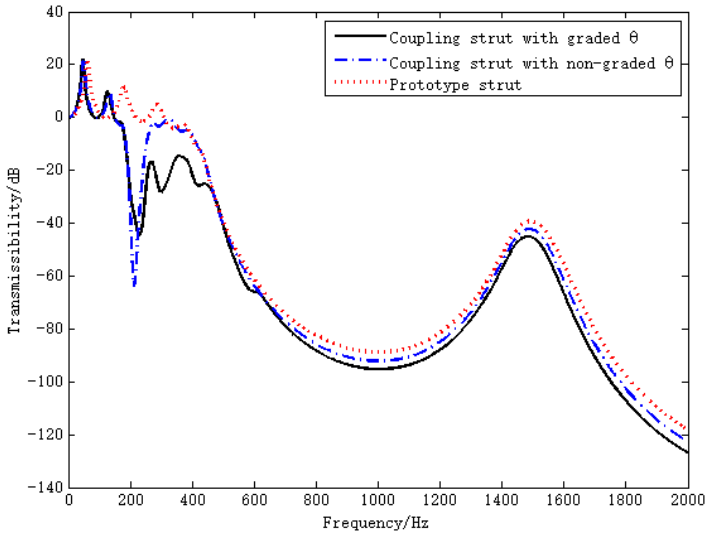


Figure 13. Transmission capability of the three types of struts when $\delta = 0.1$.

The frequency range of vibration attenuation for the coupling strut with graded θ is 152–2000 Hz, and the performance of vibration attenuation for the prototype strut starts at 307 Hz and ends at 2000 Hz. The coupling strut with graded design broadens the width of attenuation gap below 500 Hz by 155 Hz. Additionally, in the range of 152 Hz to 500 Hz, the proposed strut has better performance on vibration attenuation than the prototype one. The absolute value of the difference between the transmissibility of the two struts even reaches 43.25 dB at 226 Hz. The proposed strut not only has advantages on the band widening and vibration attenuation below 500 Hz, but also performs better than the prototype strut in the range of 500 Hz to 2000 Hz. The vibration transmissibility of the proposed strut decreases by up to 8.9 dB over the prototype strut at 2000 Hz. As the curves suggest, vibration transmission in the range of 0 Hz to 2000 Hz is substantially reduced by the graded design.

4. Conclusions

A novel type of LR/Bragg coupling periodic strut is constructed by adding parallel resonators with graded parameters to a traditional Bragg strut. Through the study of the frequency band boundaries of the infinite strut, the vibration attenuation bands of the finite strut are estimated, and the appropriate gradient parameters are derived based on the proposed method. Finally, the vibration attenuation performance of the designed strut is further optimized by introducing structural damping. The main conclusions drawn are summarized as follows:

(1) When the total mass of lead of the resonators remains the same, the parallel two resonators can generate more band gaps, which has advantages in multi-bandgap design.
(2) Under ideal infinite periodic conditions, the coupling mechanism between the LR and Bragg band gaps can be achieved by setting graded mass ratio θ.
(3) The coupling strut with graded θ widens the width of bandgap of the prototype strut by 155 Hz in the low frequency direction when the loss factor δ set to be 0.1.
(4) When the loss factor δ set to be 0.1, the proposed strut has better performance on vibration attenuation than the prototype one in the range of 152 Hz to 500 Hz, with a max improvement reaching 43.25 dB at 226 Hz.
(5) In the case of $\delta = 0.1$, the proposed strut has a significant advantage on the vibration attenuation within 500–2000 Hz. The vibration transmissibility of the proposed strut decreases by up to 8.9 dB over the prototype strut at 2000 Hz.
(6) For the coupling strut proposed in this paper, only the main constraints (e.g., simple boundary conditions, length and mass) are considered to provide the basic ideas and procedures of the design and optimization. The proposed design scheme can be easily extended to manage more complex situations as well. In future works, with an eye

on practical implementation, many other constraints should be included, such as strength, stiffness, fatigue life, and so on.

Author Contributions: Conceptualization, M.D., J.J. and F.Z.; methodology, M.D. and J.J.; validation, M.D., J.J. and F.Z.; project administration, J.J. and F.Z.; formal analysis, M.D. and J.J.; investigation, J.J., X.L. and N.S.; software, M.D.; N.S. and X.L.; resources, M.D. and F.Z.; data curation, M.D. and J.J.; visualization, X.L.; supervision, J.J. and F.Z.; funding acquisition, J.J. and F.Z.; writing—original draft preparation, M.D.; writing—review and editing, J.J. and F.Z. All authors have read and agreed to the published version of the manuscript.

Funding: This research was funded by the Foundation of National Key Laboratory of Science and Technology on Rotorcraft Aeromechanics (No. 61422202105), Qing Lan Project and National Natural Science Foundation of China (No. 51775270).

Institutional Review Board Statement: Not applicable.

Informed Consent Statement: Not applicable.

Data Availability Statement: Not applicable.

Conflicts of Interest: The authors declare no conflict of interest.

References

1. Simon, F.; Haase, T.; Unruh, O.; Pohl, M.; Tijs, E.; Wijntjes, R.; Van Der Wal, H.; Ghiringhelli, G.L. Activities of european research laboratories regarding helicopter internal noise. *Aerosp. Lab.* **2014**, *7*, 1–14.
2. Cheng, L.; Xia, Y. Review of civil aircraft cabin noise standards and control method. *Sci. Technol. Vis.* **2015**, *27*, 130.
3. Pasco, Y.; Berry, A.; Grewal, A.; Chapleau, S.L. Active control of transmission noise in a Bell 407 helicopter. In Proceedings of the 70th Annual Forum of the American Helicopter Society, Montreal, QC, Canada, 20–22 May 2014; American Helicopter Society: Fairfax, VA, USA, 2014; pp. 174–182.
4. Millott, T.A.; Yoerkie, C.A.; Welsh, W.A.; MacMartin, D.G.; Davis, M.W. Flight test of active gear-mesh noise control on the S-76 aircraft. In Proceedings of the Annual Forum Proceedings-American Helicopter Society, Washington, DC, USA, 20–22 May 1998; American Helicopter Society: Fairfax, VA, USA, 1998; pp. 241–250.
5. Sutton, T.J.; Elliot, S.J.; Brennan, M.J.; Heron, K.H.; Jessop, D.A.C. Active Isolation of Multiple Structural Waves on a Helicopter Gearbox Support Strut. *J. Sound Vib.* **1997**, *205*, 81–101. [CrossRef]
6. Maier, R.; Hoffmann, F.; Tewes, S.; Bebesel, M. Active Vibration Isolation System for Helicopter Interior Noise Reduction. In Proceedings of the 8th AIAA/CEAS Aeroacoustics Conference & Exhibit, Breckenridge, CO, USA, 17–19 June 2002; p. 2495.
7. Ma, X.J.; Lu, Y.; Wang, F.J. Active Structural Acoustic Control of Helicopter Interior Multifrequency Noise Using Input-Output-Based Hybrid Control. *J. Sound Vib.* **2017**, *405*, 187–207. [CrossRef]
8. He, C.; Zhang, F.; Jiang, J.H. Adaptive Boundary Control of Flexible Manipulators with Parameter Uncertainty Based on RBF Neural Network. *Shock Vib.* **2020**, *6*, 1–13. [CrossRef]
9. Petitjean, B.; Legrain, I.; Simon, F.; Pauzin, S. Active Control Experiments for Acoustic Radiation Reduction of a Sandwich Panel: Feedback and Feedforward Investigations. *J. Sound Vib.* **2002**, *252*, 19–36. [CrossRef]
10. Lepage, A.; Mortain, F.; Coste, L. Active Structural Acoustic Control of a Helicopter Trim Panel. In Proceedings of the Internoise 2005, the Institute of Noise Control Engineering, Rio de Janeiro, Brazil, 7–10 August 2005.
11. Flanneley, W.G. The Dynamic Antiresonant Vibration Isolator. In Proceedings of the American Helicopter Society 22th Annual Forum, Washington, DC, USA, 11–13 May 1966; pp. 152–160.
12. Braun, D. Vibration Isolator. U.S. Patent 4,619,349, 28 October 1986.
13. Peter, K. Recent Advances in Eurocopter's Passive and Active Vibration Control. In Proceedings of the American Helicopter Society 64th Annual Forum, Montréal, QC, Canada, 29 April–1 May 2008.
14. Halwes, D.R. LIVE–Liquid Inertia Vibration Eliminator. In Proceedings of the American Helicopter Society 36th Annual Forum, Washington, DC, USA, 13–14 May 1980.
15. He, C.; Lim, K.M.; Zhang, F.; Jiang, J.H. Dual-tuning mechanism for elastic wave transmission in a triatomic lattice with string stiffening. *Wave Motion* **2022**, *112*, 102951. [CrossRef]
16. Yadav, A.; Gerislioglu, B.; Ahmadivand, A.; Kaushik, A.; Cheng, G.J.; Ouyang, Z.; Wang, Q.; Yadav, V.S.; Mishra, Y.K.; Wu, Y.; et al. Controlled self-assembly of plasmon-based photonic nanocrystals for high performance photonic technologies. *Nano Today* **2021**, *37*, 101072. [CrossRef]
17. Asiri, S.; Baz, A.; Pines, D. Periodic Struts for Gearbox Support System. *J. Vib. Control* **2005**, *11*, 709–721. [CrossRef]
18. Singh, A.; Pines, D.; Baz, A. Active/Passive Reduction of Vibration of Periodic One-Dimensional Structures Using Piezoelectric Actuators. *Smart Mater. Struct.* **2004**, *13*, 698–711. [CrossRef]
19. Asiri, S.; Baz, A.; Pines, D. Active Periodic Struts for a Gearbox Support System. *Smart Mater. Struct.* **2006**, *15*, 1707–1714. [CrossRef]

20. Szefi, J.T. Helicopter Gearbox Isolation Using Periodically Layered Fluidic Isolators. Ph.D. Dissertation, Mechanical and Nuclear Engineering Department, Pennsylvania State University, University Park, PA, USA, 2003.
21. Szefi, J.T.; Smith, E.C.; Lesieutre, G.A. Formulation and Validation of a Ritz-Based Analytical Model for Design of Periodically-Layered Isolators in Compression. In Proceedings of the 19th AIAA Applied Aerodynamics Conference, Washington, DC, USA, 11–14 April 2001; p. 1684.
22. Szefi, J.T.; Smith, E.C.; Lesieutre, G.A. Formulation and Validation of a Ritz-Based Analytical Model of High-Frequency Periodically Layered Isolators in Compression. *J. Sound Vib.* **2003**, *268*, 85–101. [CrossRef]
23. Szefi, J.T.; Smith, E.C.; Lesieutre, G.A. Design and Analysis of High-Frequency Periodically Layered Isolators for Helicopter Gearbox Isolation. In Proceedings of the 44th AIAA/ASME/ASCE/AHS/ASC Structures, Structural Dynamics, and Materials Conference, Norfolk, VA, USA, 7–10 April 2003; p. 1784.
24. Szefi, J.T.; Smith, E.C.; Lesieutre, G.A. Design and Testing of a Compact Layered Isolator for High-Frequency Helicopter Gearbox Isolation. In Proceedings of the 45th AIAA/ASME/ASCE/AHS/ASC Structures, Structural Dynamics & Materials Conference, Palm Springs, CA, USA, 19–22 April 2004; p. 1947.
25. Wang, F.; Torbati, M.M.; Ma, X.; Lu, Y. Design of near-periodic struts for helicopter gearbox vibration isolation using multicell optimization. *AIAA J.* **2019**, *57*, 2634–2647. [CrossRef]
26. Wang, F.J.; Lu, Y. Research on a Gearbox Periodic Strut for Helicopter Cabin Noise Reduction. *Acta Aeronaut. Astronaut. Sin.* **2016**, *37*, 3370–3384.
27. Lu, Y.; Wang, F.J.; Ma, X.J. Research on the Vibration Characteristics of a Compounded Periodic Strut Used for Helicopter Cabin Noise Reduction. *Shock Vib.* **2017**, *2017*, 1–12. [CrossRef]
28. Lu, Y.; Wang, F.J.; Ma, X.J. Helicopter Interior Noise Reduction Using Compounded Periodic Strut. *J. Sound Vib.* **2018**, *435*, 264–280. [CrossRef]
29. Liu, Z.; Zhang, X.; Mao, Y.; Zhu, Y.Y.; Yang, Z.; Chan, C.T.; Sheng, P. Locally resonant sonic materials. *Science* **2000**, *289*, 1734–1736. [CrossRef]
30. Oudich, M.; Li, Y.; Assouar, B.M.; Hou, Z. A sonic band gap based on the locally resonant phononic plates with stubs. *New J. Phys.* **2010**, *12*, 083049. [CrossRef]
31. Goffaux, C.; Sánchez-Dehesa, J.; Yeyati, A.L.; Lambin, P.; Khelif, A.; Vasseur, J.O.; Djafari-Rouhani, B. Evidence of fano-like interference phenomena in locally resonant materials. *Phys. Rev. Lett.* **2002**, *88*, 225502. [CrossRef]
32. Liu, Z.; Chan, C.T.; Sheng, P. Three-component elastic wave band-gap material. *Phys. Rev.* **2002**, *65*, 165116. [CrossRef]
33. Wang, G.; Wen, X.; Wen, J.; Shao, L.; Liu, Y. Two-dimensional locally resonant phononic crystals with binary structures. *Phys. Rev. Lett.* **2004**, *93*, 154302. [CrossRef] [PubMed]
34. Wang, G.; Wen, J.; Wen, X. Quasi-one-dimensional phononic crystals studied using the improved lumped-mass method: Application to locally resonant beams with flexural wave band gap. *Phys. Rev.* **2005**, *71*, 104302. [CrossRef]
35. Hsu, J.C.; Wu, T.T. Lamb waves in binary locally resonant phononic plates with two-dimensional lattices. *Appl. Phys. Lett.* **2007**, *90*, 201904. [CrossRef]
36. Liang, X.; Zhang, F.; Jiang, J. Ultra-wideband outward-hierarchical metamaterials with graded design. *Int. J. Mech. Mater. Des.* **2022**, *18*, 69–184. [CrossRef]
37. He, C.; Lim, K.M.; Liang, X.; Zhang, F.; Jiang, J. Tunable band structures design for elastic wave transmission in tension metamaterial chain. *Eur. J. Mech. A/Solids* **2022**, *92*, 104481. [CrossRef]
38. Thompson, D.J. A continuous damped vibration absorber to reduce broad-band wave propagation in beams. *J. Sound Vib.* **2008**, *311*, 824–842. [CrossRef]
39. Brennan, M.J. Characteristics of a wideband vibration neutralizer. *Noise Control Eng. J.* **1997**, *45*, 201–207. [CrossRef]
40. Strasberg, M.; Feit, D. Vibration damping of large structures induced by attached small resonant structures. *J. Acoust. Soc. Am.* **1996**, *99*, 335–344. [CrossRef]
41. Nishida, E.; Koopmann, G.H. A method for designing and fabricating broadband vibration absorbers for structural noise control. *J. Vib. Acoust.* **2007**, *129*, 397–405. [CrossRef]
42. Carcaterra, A.; Akay, A.; Bernardini, C. Trapping of vibration energy into a set of resonators: Theory and application to aerospace structures. *Mech. Syst. Signal Process.* **2012**, *26*, 1–14. [CrossRef]
43. Doyle, J.F. *Wave Propagation in Structures: Spectral Analysis Using Fast Discrete Fourier Transforms. The Spectral Element Method*, 2nd ed.; Springer: Berlin/Heidelberg, Germany, 1997; pp. 152–157.
44. Lee, U.; Joohong, K.; Andrew, Y.L. Spectral element method in structural dynamics. *Shock Vib. Dig.* **2000**, *23*, 451–465. [CrossRef]
45. Xiao, Y.; Wen, J.; Wen, X. Longitudinal wave band gaps in metamaterial-based elastic rods containing multi-degree-of-freedom resonators. *New J. Phys.* **2012**, *14*, 033042. [CrossRef]
46. Jouaillec, F.; Ohayon, R. Fluid-Structure Vibration Analysis of Infinite Periodic Stiffened Cylinders. In Proceedings of the ASME/Pressure Vessels and Piping Conference, Computational Methods for Coupled Fluid-Structure Analysis, ASME, New Orleans, LA, USA, 24 June 1985; pp. 1–6.
47. Wen, J.S.; Wen, J.H.; Yu, D.L.; Wang, G.; Liu, Y.Z.; Han, X.Y. *Phononic Crystal*; National Defense Industry Press: Beijing, China, 2009.
48. Ernst, F.G. *Rubber Springs Design*; Newnes-Butterworths: London, UK, 1974.
49. Hussein, M.I.; Hulbert, G.M.; Scott, R.A. Dispersive Elastodynamics of 1D Banded Materials and Structures: Analysis. *J. Sound Vib.* **2006**, *289*, 779–806. [CrossRef]

50. Hussein, M.I.; Hamza, K.; Hulbert, G.M.; Scott, R.A.; Saitou, K. Multiobjective Evolutionary Optimization of Periodic Layered Materials for Desired Wave Dispersion Characteristics. *Struct. Multidiscip. Optim.* **2006**, *31*, 60–75. [CrossRef]
51. Wen, J.H.; Wang, G.; Yu, D.L.; Zhao, H.G.; Liu, Y.Z.; Wen, X.S. Study on the Vibration Band Gap and Vibration Attenuation Property of Phononic Crystals. *Sci. China Ser. Technol. Sci.* **2008**, *51*, 85–99. [CrossRef]